Universality classes in Coulomb blockade conductance peak-height statistics

Dayasindhu Dey and Pragya Shukla*

Department of Physics, Indian Institute of Technology, Kharagpur 721302, West Bengal, India

(Received 22 February 2014; revised manuscript received 23 August 2014; published 12 November 2014)

We investigate, using exact diagonalization techniques, the distribution of conductance peak heights in Coulomb blockade regime of a quantum dot connected to two leads under generic dot conditions. The study reveals a three-parametric dependence of the distribution: (i) two dot-lead contact characteristics and (ii) the complexity parameter, mimicking the combined effect of all dot conditions. This also indicates the presence of an infinite range of universality classes of conductance statistics, dominantly characterized just by the complexity parameter and global symmetry constraints.

DOI: 10.1103/PhysRevE.90.052118 PACS number(s): 05.40.−a, 73.63.Kv, 42.50.Lc, 73.23.−b

I. INTRODUCTION

Growing technological applications of quantum dots in diverse areas make it necessary to seek relevant criteria to characterize them for industrial production. Mesoscopic fluctuations of the dot properties require these criteria to be based not only on a single dot but an appropriate ensemble of them and therefore on the ensemble parameters. The latter, in turn, are sensitive to system conditions which could be numerous in a generic quantum dot, e.g., shape, ballistic or diffusive dynamics, elastic or inelastic scattering, *e*-*e* interaction or single-particle dynamics [1–3]. As a consequence, the characterization of the dots would be more efficient and meaningful if one can find a criteria which could classify them into various universality classes. The objective of this paper is to investigate the existence of such a criteria, namely the conductance complexity parameter [4].

Based on temperature T, mean-level spacing Δ of the dot, and width of the leads, there exist different energy regimes characterizing the dot behavior. One such regime is the Coulomb blockade ($kT < \Delta \ll e^2/C$ with C as the dot capacitance), which has evoked a lot of interest in the past due to its experimental accessibility [2]. In a recent paper [4], we derived an analytical formulation for the distribution $P(g)$ of the conductance peak heights g for a Coulomb blockade dot, under generic conditions, connected to two leads. The formulation was based on three steps: (i) the expression of the conductance of an almost closed dot in terms of the eigenvalues and eigenfunctions of the dot Hamiltonian, say, H; (ii) a system-dependent random matrix model of H in which the possibility of diverse system conditions is taken into account by considering different distribution parameters for the elements; and (iii) the complexity parametric formulation of the eigenvalue or eigenfunction statistics [5,6]. Our analysis led to a diffusion equation for $P(g)$ which is governed only by three parameters, namely the complexity parameter Λ_g for the conductance, a dot-lead parameter, and the effective size N of the dot Hamiltonian (see Eq. (71) of Ref. [4]). In the limit $N \to \infty$, the size dependence can be removed by rescaling the conductance, which leaves only Λ_g as the diffusion parameter for a fixed set of leads. As in general the dot Hamiltonian is of infinite size, this implies an analogous behavior of $P(g)$ for the dots with the same Λ_g value and under same set of global constraints although their physical conditions, e.g., shape, disorder, or boundary conditions, may differ. A global constraint here refers to a condition which defines the nature of the H matrix; for example, H is a real-symmetric matrix in the presence of the time-reversal symmetry [6].

The diffusion equation in Ref. [4] was derived only for a particular class of global constraints, namely the dots with time-reversal symmetry. It was also based on some approximations, e.g., weak correlations between the eigenvalues and the eigenfunctions, etc., and its complete solution for different initial conditions is yet to be obtained. An exact formulation of Λ_g is also required. Furthermore, theoretical claim of the system-complexity manifesting itself in the physical properties through a single parameter [4] has deep implications and its thorough numerical verification for various statistical properties is very desirable. This motivates us to pursue the numerical analysis of the influence of dot conditions as well as global constraints on the conductance fluctuations and verify the analytical claims of Ref. [4].

The paper is organized as follows. Sections IIA and IIB briefly review the theoretical complexity parameter formulation of the Coulomb blockade dot conductance (with details given in Ref. [4]), along with a derivation of the moments of the peak-height distribution as a function of complexity parameter in Sec. II C. Section III describes the two prototypical ensembles used to model generic dot Hamiltonians and their complexity parameters Λ_g under different symmetry conditions. The detailed numerical analysis of the conductance peak-height distribution and its Λ_g dependence for different combinations of global and local constraints is discussed in Sec. IV; the numerics not only confirms the theoretical predictions for the dots with time-reversal symmetry but also indicates their validity for dots without this symmetry (no theory available so far) and clarifies many other details. Section V gives an outline of the possible experiments which could be performed to verify the complexity parametric formulation. We conclude in Sec. VI with a summary of our main results.

II. CONDUCTANCE DISTRIBUTION: DIFFUSION DUE TO VARYING DOT CONDITIONS

A. Conductance peak height for a single dot

The electron dynamics inside a disordered quantum dot weakly coupled to two leads can be described by the

*Corresponding author: shukla@phy.iitkgp.ernet.in

Hamiltonian [7] $H = H_{\rm dot} + H_{\text{dot-lead}}$. Here

$$H_{\rm dot} = -\frac{\Delta^2}{2m} + V(\mathbf{r}) \tag{1}$$

is the dot Hamiltonian with a potential $V(\mathbf{r})$ containing the effect of confining dot boundaries and random impurities. The interaction $H_{\text{dot-lead}}$ of the dot with two leads is described by a discrete set of points

$$H_{\text{dot-lead}} = \frac{i\Omega\Delta}{2\pi}\left[\kappa_l \sum_{\mathbf{r}_L \epsilon A_L} \delta(\mathbf{r}-\mathbf{r}_L) + \kappa_r \sum_{\mathbf{r}_R \epsilon A_R} \delta(\mathbf{r}-\mathbf{r}_R)\right] \tag{2}$$

with Ω as the dot volume and Δ as the mean-level spacing of $H_{\rm dot}$. The symbols A_L, A_R refer to the left and right lead and κ_l, κ_r as the dimensionless coupling parameters; a weak dot-lead coupling can be modeled by taking $0 < \kappa_l, \kappa_r \ll 1$, although small but nonzero coupling leads to finite width of energy levels of the dot which is caused by local fluctuations of the electron wave function in the dot-lead contact regions.

Assuming the dot geometry to consist of a two-dimensional lattice of N sites, $H_{\rm dot}$ can be represented by a finite $N \times N$ matrix in the site basis $|n\rangle$ with $n = 1,2,\ldots N$:

$$H_{\rm dot} = \sum_{m,n=1}^{N} H_{mn} a_m^\dagger a_n. \tag{3}$$

Here $a_n^\dagger, a_n$ as the creation and annihilation operator of an electron at the $n^{\rm th}$ site: $|n\rangle = a_n^\dagger|0\rangle$ (with $|0\rangle$ as the vacuum state). The two leads connected to dot are placed at two sets of fixed sites [7]. The pointlike leads or single channel leads (i.e., when the typical size of the contact is smaller than the area λ^{d-1} with λ as the electron wavelength) are represented by the two sites at the dot boundary. The case of M-channel leads can be treated by choosing two sets of M closely spaced sites (although far enough apart to have negligible site-site correlations). Due to weak coupling, the eigenfunctions of the dot Hamiltonian are unaffected by the leads.

The total width Γ of the energy level E_ψ of $H_{\rm dot}$ with an eigenfunction $\Psi(r)$ ($H\Psi = E_\psi \Psi$) to decay into the leads is the sum over contributions from the left and right leads as follows: $\Gamma = \Gamma_l + \Gamma_r$. As each lead can support several channels, this leads to [2]

$$\Gamma_t = \sum_c |\gamma_{tc}|^2 \qquad (t = l,r). \tag{4}$$

Here γ_{tc} is the partial amplitude to decay into channel c in the lead "t," which can be expressed as $\gamma_{tc} = \langle \phi_c|\Psi\rangle$ with ϕ_c as the channel wave function. In general, the decay width of a level into different channels can differ as well as be correlated; as a consequence, ϕ_c is in general not orthogonal and can have different norms. This leads to the introduction of the channel correlation matrix M^{ts} $(t,s = l,r)$ with its elements as $M^{ts}_{cc'} = \frac{1}{N}\langle \phi_c|\phi_c'\rangle$.

If the dot-lead contacts are assumed to be lines and the channels to be extended, the scalar product is then defined over the dot-lead interface [2]. But if the leads are assumed to be composed of several point contacts $\mathbf{r}_c$, then each one of them constitutes one channel and the related partial width is $\gamma_{tc} = (\frac{\kappa_t \Omega\Delta}{\pi})^{1/2}\Psi(\mathbf{r}_c)$. This gives $\Gamma_t = \frac{\kappa_t\Omega\Delta}{\pi}\sum_{\mathbf{r}_t \epsilon A_t} |\Psi(\mathbf{r}_t)|^2$. Note in the point contact model, $M_{cc'}$ is a measure of the spatial wave-function correlations at two different points.

The weak dot-lead coupling (e.g., $\kappa_l, \kappa_r \ll 1$) leads to smaller level widths compared to their mean level spacing Δ. As a consequence, the significant contribution to conductance comes only from the resonance Ψ with energy E_Ψ closest to the scattering energy E of the electron. Further, at low temperature $kT < \Delta$, only one level participates in the conduction. Thus, in the Coulomb-blockade regime $\overline{\Gamma} \ll T \ll \Delta$ (with $\overline{\Gamma}$ as the average width), the transport occurs only by the resonant tunneling through the corresponding energy level of the dot. The single-level conductance peak height g (measured in units of $\frac{e^2}{h}\frac{\pi}{2kT}$) in this case can be given as [2]

$$g = \frac{\Gamma_l \Gamma_r}{\Gamma_l + \Gamma_r}. \tag{5}$$

B. Conductance peak height distribution for a dot ensemble

The weak dot-lead coupling leads to Coulomb blockade oscillations of the peak heights as a function of the gate voltage. A detailed information about these oscillations can be obtained from the distribution of peak heights and peak spacings. At low temperatures $kT \leqslant \Delta$, the exponential suppression of thermal correlations among peaks and the weak sensitivity of an individual peak to dynamical correlations [2], allows one to consider the peak-height distribution of each resonance separately. As clear from Eqs. (4) and (5), the distribution $P_g(g)$ of g can be obtained from the joint distribution $P_\Gamma(\Gamma_l,\Gamma_r)$ of the resonance widths which in turn is derived from the components of the eigenfunction Ψ. This approach was used in Ref. [4] to derive a diffusion equation for $P_g(g)$ (see Eq. (62) of Ref. [4]) for an ensemble of the dot Hamiltonians under generic conditions. To make this work self-contained, we briefly review here the crucial steps of the derivation (see Ref. [4] for the details).

We consider an ensemble of the dot Hamiltonians described by the probability density,

$$\rho(H) = C\exp\left[-\sum_{s=1}^{\beta}\sum_{k,l=1;k\leqslant l}^{N} \frac{1}{2h_{kl;s}}(H_{kl;s} - b_{kl;s})^2\right], \tag{6}$$

with C as the normalization constant, h_s and b_s as $N \times N$ matrices of the variances $h_{kl;s} = \langle H^2_{kl;s}\rangle - \langle H_{kl;s}\rangle^2$ and mean values $b_{kl;s} = \langle H_{kl;s}\rangle = \langle V_{kl;s}\rangle$, respectively. Here $\beta = 1,2$ for H real and complex Hermitian, respectively, and the subscript s refers to the real ($s = 1$) or imaginary ($s = 2$) part of a complex variable. For different choices of the h,b matrices, Eq. (6) can mimic the dots under different conditions.

The variation of system conditions, e.g., gate voltage, disorder strength, and particle density, may result in a variation of the distribution parameters $\{h,b\}$ and therefore an evolution of the H ensemble. As discussed in Refs. [6,8,9], under a change of parameters $h_{kl} \to h_{kl} + \delta h_{kl}$ and $b_{kl} \to b_{kl} + \delta b_{kl}$, $\rho(H)$ undergoes a diffusion dynamics along with a finite drift, and, using Gaussian nature of $\rho(H)$, it can exactly be shown that

$$T\rho = L\rho, \tag{7}$$

where T is a combination of $M = N(N+1)$ parametric derivatives and L is a diffusion operator in matrix space: $T = \sum_{k\leqslant l;s}[(g_{kl} - 2\gamma h_{kl;s})\frac{\partial}{\partial h_{kl;s}} - \gamma b_{kl;s}\frac{\partial}{\partial b_{kl;s}}]$ and $L = \sum_{kl;s}\frac{\partial}{\partial H_{kl;s}}[\frac{g_{kl}}{2}\frac{\partial}{\partial H_{kl;s}} + \gamma H_{kl;s}]\rho$ with $g_{kl} = 1 + \delta_{kl}$. Here γ is an arbitrary parameter, giving the variance of the matrix elements at the end of the evolution [8,9]. A suitable transformation of parametric space $\{h,b\}$ to $\{y_1,\ldots,y_M\}$ maps T to a single parametric derivative, $T\rho = \frac{\partial\rho}{\partial Y}$ with $Y \equiv y_1$, which in turn reduces Eq. (8) to a single parametric diffusion (see Appendix A or Refs. [6,8,9] for details)

$$\frac{\partial\rho}{\partial Y} = L\rho. \tag{8}$$

Here

$$Y = \frac{-1}{\beta N^2\gamma}\sum_{k\leqslant l}\left[\sum_{s=1}^{\beta}\ln|1-\gamma(2-\delta_{kl})h_{kl;s}| + \ln\left|\sum_{s'=1}^{\beta}b_{kl;s'} + \delta_{b0}\right|^2\right] + C_y \tag{9}$$

with C_y as an arbitrary constant and $\delta_{b0} = 1$ if both $b_{kl;1} = b_{kl;2} = 0$ else $\delta_{b0} = 0$. Note, as mentioned in Appendix A, the $T \to \frac{\partial}{\partial Y}$ transformation is based on the condition that the transformed variables $y_2,\ldots,y_M$ remain constant throughout the evolution. These $M-1$ constants originate from the global constraints imposed on the system which affect the nature (e.g., transformation properties) of each H matrix in the $\rho(H)$ ensemble. (Thus global constraints can also be referred as the "matrix constraints.") For example, each H matrix is real-symmetric in presence of time-reversal symmetry and complex Hermitian in its absence, the dimensionality along with hopping conditions in the system gives rise to same degree of sparsity for each H matrix. The systems with similar global constraints, however, may have different local constraints which in a suitable ensemble must manifest through the ensemble parameters. For example, the Anderson ensemble and Brownian ensemble, described later in this paper, have same global constraints but different ensemble parameters. As Y is a combination of all ensemble parameters, it contains information of all local constraints on the system. Thus Eq. (8) implies that systems with same global constraints but different local constraints will lie on a path characterized by $y_2,\ldots,y_M$.

Equation (8) is derived for arbitrary initial conditions of the matrices h_s, b_s. In y space this corresponds to an arbitrary of initial condition with respect to Y while keeping the parameters $y_2,\ldots,y_M$ constants. Alternatively, the systems lying on a path fixed by a set of global constraints can always be accessed from a common initial condition.

A direct integration of Eq. (8) over undesired eigenvalues and eigenfunctions of H gives a Y-governed diffusion of the rest of them. But the diffusion equation contains integrals which require a prior information about the eigenvalues-eigenfunctions correlations. The further progress can then be made only by approximations. As discussed in detail in Ref. [5], the diffusion equation of the joint probability distribution $P_\Psi(\Psi) \equiv P_{N1}(\psi_1,\ldots,\psi_N)$ of the components ψ_j, $j = 1 \to N$ of an eigenfunction Ψ of H can be reduced in a closed form if the eigenvalues and eigenfunction are assumed to be weakly correlated (see Appendix A). The approximation gives

$$\frac{\partial P_\Psi}{\partial\Lambda_\Psi} = \sum_{n=1}^{N}\frac{\partial}{\partial\psi_n}\left[(N-1)\psi_n + \sum_{m=1}^{N}\frac{\partial}{\partial\psi_m}(\delta_{mn} - \psi_n\psi_m)\right]\times P_\Psi, \tag{10}$$

where $\Lambda_\Psi = (\chi/2)\Lambda_e$ with χ related to the average localization length ξ of the eigenfunction Ψ and Λ_e as the rescaled complexity parameter,

$$\Lambda_e(E,Y) = \frac{Y - Y_0}{\Delta^2_{\rm local}}, \tag{11}$$

with Y and Y_0 as the complexity parameters for the ensemble and its initial state [5], $\Delta_{\rm local}$ as the *local* mean level spacing of the d-dimensional dot Hamiltonian ($N = L^d$),

$$\Delta_{\rm local}(E) \approx L^d\xi^{-d}\Delta(E) \tag{12}$$

with $\xi(E)$ as the average localization length at an energy E [9]. The proportionality factor χ in Eq. (19) depends on the eigenfunction statistics and is known approximately [5],

$$\chi \sim \mu\xi^{-d} \quad \text{for} \quad \mu\xi^{-d} > 1, \qquad = 1 \quad \text{for} \quad \mu\xi^{-d} < 1, \tag{13}$$

where $\mu = [e^{2\gamma(Y-Y_0)} - 1]^{-1}$.

Equation (4) along with Eq. (10) leads to the diffusion equation for the resonance width distribution $P_\Gamma(\Gamma_l,\Gamma_r)$ for the resonance Ψ; the steps of the derivation are discussed in detail in Ref. [4]. As expected, the exact diffusion equation again contains various sums related to the channel-channel correlations. To reduce the equation in a closed form, following approximations are applied as follows: (i) The channel correlation matrices $M^{(ll)}, M^{(rr)}$ for the left and right leads are assumed to be *effectively* diagonal. This is because, in general, the correlations between different channels on the same lead are expected to be relatively weak as compared to self-correlations, that is, $M^{(tt)}_{pp} \gg M^{(tt)}_{pq}$ with p,q as two channels on the lead "t." (ii) The cross-correlation matrix M^{lr} among the channels on left and right leads is also assumed to be effectively diagonal. These approximations give

$$\frac{1}{4}\frac{\partial P_\Gamma}{\partial\Lambda_\psi} = \sum_{t=l,r}\frac{\partial}{\partial\Gamma_t}\left[\frac{\partial}{\partial\Gamma_t}[\Gamma_t(\alpha_t - \Gamma_t)P_\Gamma] + \frac{1}{2}(N\Gamma_t - N_t\alpha_t)P_\Gamma\right] + 2\frac{\partial^2}{\partial\Gamma_l\partial\Gamma_r}[\alpha_c\sqrt{\Gamma_l\Gamma_r} - \Gamma_l\Gamma_r]P_\Gamma, \tag{14}$$

where α_t is the average diagonal element of the channel matrix of the lead "t" with N_t channels, where $t = l,r$: $\alpha_t = \overline{\langle\Phi^t_p|\Phi^t_p\rangle} = \frac{1}{N_t}\sum_p M^{(tt)}_{pp} = \frac{1}{N_t}{\rm Tr}M^{tt} = \overline{M^{tt}_{pp}}$ with the symbol $\overline{x_p}$ implying average of x_p over p. Similarly, $\alpha_c = \langle M^{lr}_{pq}\rangle_{p,q}$ is the average matrix element of the left-right (lr) channel matrix. Note, for later reference, for the point contact model described by the dot-lead Hamiltonian [Eq. (2)],

$$\alpha_l = \frac{\Delta}{\pi}\kappa_l, \quad \alpha_r = \frac{\Delta}{\pi}\kappa_r, \quad \alpha_c = \frac{\Delta}{\pi}\sqrt{\kappa_l\kappa_r}. \tag{15}$$

Partial integration of Eq. (14) now gives the diffusion equation for

$$P_g(g) = \int \delta\left(g - \frac{\Gamma_l\Gamma_r}{\Gamma_l+\Gamma_r}\right) P_\Gamma d\Gamma_l d\Gamma_r$$

of the dots under generic conditions, with a nonzero correlation between left and right leads (see Ref. [4] for details of the derivation),

$$\frac{\partial P_g}{\partial \Lambda_g} = \frac{\partial^2}{\partial g^2}\{g(s-g)P_g + Q_2\} + \frac{1}{2}\frac{\partial}{\partial g}\{(Ng-\theta)P_g + 2Q_1\}, \tag{16}$$

where $\theta = \frac{1}{2}(N_l\alpha_l + N_r\alpha_r), \phi = \frac{1}{2}(N_l\alpha_l - N_r\alpha_r), s = \frac{1}{2}(\alpha_l + \alpha_r), u = \frac{1}{2}(\alpha_l - \alpha_r)$, and

$$Q_n(g) = g^{2n}\int \delta\left(g - \frac{\Gamma_l\Gamma_r}{\Gamma_l+\Gamma_r}\right)(\Gamma_l\Gamma_r)^3 v_n(\Gamma_l,\Gamma_r) \times P_\Gamma d\Gamma_l d\Gamma_r, \tag{17}$$

with $n = 1,2$ and

$$\begin{aligned} v_1(x,y) &= (\theta+2s)x^2y^2 - xy(x+y)^{-1}[2\Omega_0 xy \\ &\quad + 2u(y^3-x^3)] - (\phi+4u)(y^2-x^2)xy/2 \\ v_2(x,y) &= xy[\Omega_0 - 3s(x+y)] + u(y^3-x^3), \end{aligned} \tag{18}$$

where $\Omega_0 = 2\alpha_c\sqrt{xy}$. Here $\Lambda_g(E,Y)$ is the conductance complexity parameter

$$\Lambda_g = 2\chi\Lambda_e, \tag{19}$$

with Λ_e given by Eq. (11). In general, it is difficult to express Q_n as functions of g only but it can be achieved by the system-specific approximations. As discussed in Ref. [4], for the case of approximately linear relation between left and right resonance width, namely $\Gamma_r = q\Gamma_l$ (with q fluctuating over the ensemble), Eq. (16) reduces to an equation for $P_g(g;q)$. An ensemble average of $P_g(g;q)$ over q then gives the diffusion equation for $P_g(g)$ as follows:

$$\frac{\partial P_g}{\partial \Lambda_g} = \frac{\partial^2}{\partial g^2}[g(t_2-g)]P_g + \frac{1}{2}\frac{\partial}{\partial g}[Ng - t_1]P_g \tag{20}$$

with t_1, t_2 as the dot-lead parameters,

$$\begin{aligned} t_1 &= \theta - 2(\theta+2s)\frac{(\eta-1)}{\eta^2} + 8\alpha_c\frac{(\eta-1)^{3/2}}{\eta^3} \\ &\quad + 4u\frac{[1-(\eta-1)^3]}{\eta^3} + 2(\phi/2+2u)\frac{(2-\eta)}{\eta} \\ t_2 &= 2\alpha_c\frac{(\eta-1)^{3/2}}{\eta^3} + s\left[1 - 3\frac{(\eta-1)}{\eta^2}\right] + u\frac{[1-(\eta-1)^3]}{\eta^3}, \end{aligned} \tag{21}$$

with $\eta = 1 + \langle q\rangle^{-1}$ and $\langle q\rangle$ as the ensemble-average value of q. For example, for the symmetric leads with $N_l = N_r = N_c$ channels, one has $\langle\Gamma_l\rangle = \langle\Gamma_r\rangle$ and $\alpha_l = \alpha_r = \alpha_c$ and $\eta = 2$, which corresponds to $\theta = N_c s = N_c\alpha_l, \phi = N_c u = 0$. Equation (21) then gives, for the symmetric leads,

$$t_1 = \tfrac{1}{2}N_c\alpha_l, \quad t_2 = \tfrac{1}{2}\alpha_l. \tag{22}$$

Equation (20) describes the diffusion of peak-height distribution of a Coulomb blockade dot under varying dot-leads conditions while preserving the time-reversal symmetry. As clear from the equation, the diffusion is governed by three parameters Λ_g and t_1, t_2; the information about the dot conditions, e.g., shape, disorder, and interaction strength, are contained in Λ_g, while t_1, t_2 depend on the dot-lead contact characteristics. For the fixed values of t_1, t_2, therefore, the dots with different conditions (but same global constraints) are expected to show same behavior of $P(g)$ as long as their Λ_g are equal. Furthermore, in the large-g regime ($g > t_1/N, t_2$), Eq. (20) becomes almost independent of t_1, t_2; the evolution of $P_g(g)$ in the regime, in different dots under variation of system conditions, should therefore be analogous irrespective of the dot-lead contact characteristics. An important point to note here is the Δ dependence of Λ_g, t_1, t_2. For the cases where varying system-conditions lead to localization to delocalization transition, $\Delta_{\rm local}$ changes more rapidly as compared to Δ. As Λ_g depends on $\Delta_{\rm local}$, it is more sensitive to the variation of system conditions as compared to t_1, t_2 which depend on Δ only. Thus during a Λ_g governed evolution, t_1, t_2 can be treated as almost constant.

The next desirable step is to solve Eq. (20). In Ref. [4], a partial solution for an arbitrary initial condition was obtained by mapping the equation to the hypergeometric equation and then analyzing it near the singularity at $g = 0$,

$$P(g,\Lambda_g) = t_2^{-1}\sum_{m=0}^{\infty} B_m d_m e^{-\frac{1}{2}(N+2m-2)m\Lambda_g} e^{-Ng/2t_2}(g/t_2)^{1-c} \times L_m^{1-c}(Ng/2t_2), \tag{23}$$

where $d_m = \frac{\Gamma(m+1)\Gamma(2-c)}{\Gamma(m+2-c)}$ and $B_m = (\frac{N}{2})^{2-c}\frac{1}{\Gamma(2-c)}\int L_m^{1-c}(Nz/2)P(z,0)dz$. For example, for the initial condition, namely $P_g(g;0) = \delta(g)$, the series in Eq. (23) can be reduced to a simple form,

$$P(g,\Lambda_g) = \frac{N}{2\Gamma(2-c)t_2\tau}\left(\frac{Ng}{2t_2\tau}\right)^{1-c} e^{-Ng/2t_2\tau}, \tag{24}$$

with $\tau = 1 - e^{-N\Lambda_g/2}$ as a function of dot parameters $t_2, c = 2 - \frac{t_1}{2t_2}$ as the lead parameters. Note $\Lambda_g \to \infty$ corresponds to the Gaussian orthogonal ensemble (GOE) result [2].

A complete solution of the Eq. (20) for all g regimes is yet to be obtained; it requires a thorough analysis near all the three singularities of hypergeometric equation and the connection formulas for $P_g(g)$ behavior in various regions. Furthermore, Ref. [4] derives the conductance diffusion equation for a dot ensemble with time-reversal symmetry. The diffusion equations for other symmetry consideration is not yet known although such a possibility is indicated by the existence of the complexity-parametric formulation of the eigenfunctions for these cases (see Refs. [5,10]). This motivates us to pursue a detailed numerical analysis of the dot ensembles, both with as well as without time-reversal symmetry, and subjected to variation of the ensemble parameters from different initial conditions. The objective is not only to verify our theoretical claim about complexity parameter characterized universality of the peak-height statistics for generic quantum dots but also gain insight for the cases where either an equation of type (20) is not yet formulated or its solution is not available. The

numerical analysis would also help us in verifying various approximations used in the derivation as well as to analyze relative influence of the dot-lead parameters t_1, t_2.

C. Moments of the peak-height distribution

In experimental as well as numerical studies on quantum dots, a calculation of moments of $P_g(g)$ is relatively easier and is a better tool to probe complexity parametric formulation. The n^{th} moment defined as $M_n \equiv \langle g^n \rangle = \int_0^\infty g^n P(g) dg$ can directly be obtained from Eq. (20) in the following steps. Multiplication of Eq. (20) by g^n and subsequent integration gives M_n as a function of Λ_g,

$$2\frac{\partial M_n}{\partial \Lambda_g} = n[2t_2(n-1)+t_1]M_{n-1} - n(2n-2+N)M_n. \quad (25)$$

Solving Eq. (25) gives a hierarchical set of relations for the moments

$$M_n(\Lambda_g) = e^{-b_0\Lambda_g}\left[M_n(0) + \frac{n}{2}(2t_2(n-1)+t_1) \times \int_0^{\Lambda_g} M_{n-1}(\Lambda_g) e^{b_0\Lambda_g} d\Lambda_g\right], \quad (26)$$

where $b_0 = \frac{n}{2}(2n-2+N)$. Equation (26) can now iteratively be used to obtain M_n. For example, for $n = 1$, it gives the ensemble averaged peak height $M_1 \equiv \langle g \rangle$ a function of Λ_g,

$$\langle g(\Lambda_g)\rangle = \frac{1}{N}[t_1 - (t_1 - N\langle g(0)\rangle)e^{-N\Lambda_g/2}], \quad (27)$$

with $\langle g(0)\rangle$ as the average peak height at $\Lambda_g = 0$. Similarly, a self-consistent equation for the variance $\sigma^2 \equiv M_2 - M_1^2$ can be derived from Eq. (26) as follows:

$$\sigma^2(\Lambda_g) = e^{-N\Lambda_g}\left[\sigma^2(0) + 2\int_0^{\Lambda_g}(t_2 - \langle g(x)\rangle)\langle g(x)\rangle e^{Nx} dx - 2\int_0^{\Lambda_g}\sigma^2(x)e^{Nx}dx\right]. \quad (28)$$

As discussed in Sec. V, Λ_g can experimentally be determined by a measurement of $\langle g(\Lambda)\rangle$ and using Eq. (27). Further Eqs. (27) and (28) relate the average peak height and variance at $\Lambda_g \to \infty$ to dot-lead contact characteristics t_1, t_2,

$$\langle g(\infty)\rangle = \frac{t_1}{N}, \quad \sigma^2(\infty) = \frac{2t_2}{N}\langle g(\infty)\rangle. \quad (29)$$

As clear from the above, an experimental measurement of $\langle g(\infty)\rangle$ and $\sigma^2(\infty)$ would give information about t_1, t_2. The later along with Eqs. (21) and (15) can then be used to obtain dot-lead coupling parameters κ_l, κ_r; for example, for the symmetric leads with single channel, Eqs. (22) and (15) gives $\kappa_l = \kappa_r = 2\pi\Delta t_1 = 2\pi\Delta t_2$.

III. ENSEMBLES OF DOT HAMILTONIANS

To numerically verify Λ_g dependence of $P_g(g)$, we consider two different ensembles for the dot Hamiltonian along with a possibility of the time-reversal symmetry breaking. Both ensembles can be represented by the probability density Eq. (6) but their distribution parameters $h_{kl;s}, b_{kl;s}$ differ. Our choice of the ensembles is dictated by the reason (i) the models are prototype of many physical systems related to different areas and (ii) a comparative study of the eigenvalue fluctuations of these models, verifying single parametric dependence has already been carried out, with corresponding complexity parameters and other results given in Ref. [9].

The two ensembles can be described as follows.

A. Anderson ensemble (AE)

Our first choice is an ensemble of the standard Anderson Hamiltonians H which describes the electron dynamics in a disordered lattice within an independent electron approximation. In the tight binding representation, H for a two-dimensional lattice of linear size L ($d = 2, N = L^2$), with a Gaussian site disorder (of variance $w^2/12$ and mean zero), an isotropic, nonrandom hopping u to z nearest neighbors, and periodic boundary conditions, is given by Eq. (3). The ensemble density in this case can be described by Eq. (6) with

$$h_{kk} = \frac{w^2}{12}, \quad b_{kk} = 0, \quad h_{kl} = 0, \quad b_{kl} = uf(kl), \quad (30)$$

where $f(kl) = 1$ for $\{k,l\}$ nearest-neighbor site pairs, $f(kl) \to 0$ for all disconnected site-pairs. This dot has the time-reversal symmetry which is broken in the presence of an Aharonov Bohm flux ϕ. The flux gives rise to a nonzero hopping $H_{kl} = u\exp(i\phi)$ for all nearest-neighbor site pairs k,l. Choosing ϕ to be nonrandom implies $b_{kl;s} = u_s f(kl)$, where $u_1 = u\cos\phi, u_2 = u\sin\phi$. As clear, the Anderson Hamiltonian contains many system parameters, e.g., system size L, on-site disorder w, hopping u, and flux ϕ. The ensemble complexity parameter Y in this case is [9]

$$Y = \frac{-1}{\beta N\gamma}\ln\left[\left|1 - \frac{\gamma w^2}{12}\right||u_1 + u_2 + \delta_{u_1 0}\delta_{u_2 0}|^{z/2}\right] + C_y, \quad (31)$$

where $z = 4$.

[Note, as briefly mentioned in the previous section, during Y-governed diffusion of $P_g(g)$, the rest $M-1$ parameters $y_2, \ldots, y_M$ act as independent constants of dynamics. Although not required for analysis, it is relevant to know them. For the AE case, $N(N-1-z)$ of these constants can be identified with those off-diagonals which are not connected by hopping and remain zero throughout the diffusion. The choice of the remaining $(2+z)N$ constants depends on the nature of the system conditions subjected to variation. For example, if the hopping remains isotropic and on-site disorder is the same for all sites, the remaining constants can then be obtained from the difference of the variances and mean values of the pairs of diagonals and hopping off-diagonals.]

The variations of system condition governed by w, u, and ϕ can lead to three different types of statistical crossovers in the spectra as well as the eigenfunctions of the Anderson ensemble, which in turn manifests in $P_g(g)$, too. Referring the $P_g(g)$ crossovers by their spectral counterpart, these can be described as follows:

(i) *Poisson* $\to$ *GOE*: The choice of a large w/u ratio as the initial condition in AE corresponds to an insulator state with the spectral statistics given by the Poisson universality class [2,9,11]. A decrease of w while keeping $\phi = 0$ fixed leads to an evolution of the ensemble in a real-symmetric matrix space and a crossover of the spectral statistics from Poisson $\to$ GOE [9].

Choosing an insulator initial state $w = \sqrt{6}/\gamma, u = 1, \phi = 0$, Eq. (31) then gives $Y_0 = -\frac{1}{\beta N \gamma}\ln 2 + C_y$ and, with $\beta = 1$ and γ very small,

$$Y - Y_0 = \frac{-1}{\beta N \gamma}\ln\left(2\left|1 - \frac{\gamma w^2}{12}\right|\right). \tag{32}$$

The global constraint in this case is time-reversal symmetry.

(ii) *Poisson → Gaussian unitary ensemble (GUE)*: A decrease of disorder w while keeping ϕ fixed at a nonzero value, say, ϕ_0, leads to an evolution of ensemble in absence of time-reversal symmetry and results in a crossover of the spectral statistics from Poisson → GUE [9]. Here Poisson initial state can be achieved by choosing $w = \sqrt{6}/\gamma, u_1 = \cos\phi_0, u_2 = \sin\phi_0$. The complexity parameter $Y - Y_0$ in this case again turns out to be the same as in Eq. (32) but now $\beta = 2$. Here the global constraint is absent the time-reversal symmetry.

(iii) *GOE → GUE*: Contrary to the previous two cases, w in this case is kept fixed at a very small value (in metallic regime) and ϕ is varied nonrandomly beyond its initial value $\phi = 0$. A weak disorder and zero flux results in a GOE-type level statistics of the initial state [2,9]. A slow violation of the time-reversal symmetry in the presence of weak disorder results in a statistical crossover of the ensemble from GOE to GUE [9]. For a GOE initial state (w, $\phi = 0$), Eq. (31) now gives $Y_0 = -\frac{1}{2\gamma N}\ln|1 - \gamma w^2/12| + C_y$,

$$Y - Y_0 = \frac{-1}{2N\gamma}\ln|\cos(\phi) + \sin(\phi)|. \tag{33}$$

Here again the global constraint is absent the time-reversal symmetry but now the initial state differs from that of case (ii).

B. Brownian ensemble (BE)

Our second choice is an ensemble of dot Hamiltonians modeled by a Brownian ensemble which describes a nonstationary state of the matrix elements undergoing a crossover due to a random perturbation of a stationary ensemble, say, H_0, by another one (see Ref. [9] and references therein). For comparison with the Anderson case, we consider BEs with same global symmetry, namely those appearing during a transition from Poisson to GOE or GUE and from GOE to GUE. The BEs for all three cases can be described by a $N \times N$ ensemble H represented by Eq. (1) with ensemble parameters

$$\begin{aligned}\left\langle H^2_{kl;s}\right\rangle &= h_{kl;s} = \frac{1}{4\gamma}\left[2\delta_{kl} + \frac{\gamma(1-\delta_{kl})}{1 + c_s N^2}\right].\\ \langle H_{kl;s}\rangle &= b_{kl,s} = 0,\end{aligned} \tag{34}$$

Using Eq. (34) in Eq. (9), Y for the intermediate BE case turns out to be

$$Y \approx \frac{1}{\gamma\beta N}\left[\ln 2 + \frac{\gamma}{4}\frac{(2 + c_1N^2 + c_2N^2)}{(1 + c_1N^2)(1 + c_2N^2)}\right] + C_y. \tag{35}$$

(In this case, the constants $y_2, \ldots, y_M$ are trivial and can be chosen as zero, which corresponds to identifying them, for example, with different variances of the pairs of off-diagonals as well as pairs of mean values.)

Here again, the variation of parameters c_1, c_2 can lead to three types of crossover (again referring them by their spectral counterparts) as follows:

(iv) *Poisson → GOE*: As is clear from Eq. (34), the case $c_1, c_2 = \infty$ corresponds to an ensemble of diagonal matrices with Poisson spectral statistics. Starting from this state, a variation of c_1 for a fixed $c_2 = \infty$ leads to Poisson → GOE crossover [9]. Equation (35) then gives $Y_0 = \frac{1}{\gamma\beta N}\ln 2 + C_y$ (with $\beta = 1$),

$$Y - Y_0 = \frac{1}{4c_1N^2}. \tag{36}$$

As is clear, the global constraint class in this case is same as for AE case (i).

(v) *Poisson → GUE*: Starting again from $c_1, c_2 = \infty$, a variation of both c_1, c_2 leads to this crossover; keeping $c_1 = c_2$ during the variation, Eq. (35) again gives same $Y - Y_0$ as in Eq. (36) (but now $\beta = 2$). The global constraint here is same as for the AE cases (ii) and (iii) but the initial condition is analogous (statistically) to that of AE case (ii).

(vi) *GOE → GUE*: For $c_1 = 0, c_2 = \infty$, Eq. (34) describes a GOE ensemble. A decrease of c_2 now for a fixed $c_1 = 0$ then leads to a GOE → GUE crossover [2,9] with $Y_0 = \frac{1}{2\gamma N}[\ln 2 + \frac{\gamma}{4}] + C_y$ and

$$Y - Y_0 = \frac{1}{8c_2N^2}. \tag{37}$$

Again the global constraint here is same as for the AE case (ii) and (iii) but the initial condition is analogous to that of AE case (iii).

IV. $P_g(g)$ CALCULATION: EXACT DIAGONALIZATION OF DOT ENSEMBLES

The objective of our numerical analysis is twofold:

(1) to find whether the peak-height distributions for AE and BE, both belonging to a same global symmetry class, are analogous at their respective dot conditions which satisfy $\Lambda_{g,a} = \Lambda_{g,b}$ (with subscripts a,b referring to AE and BE, respectively), and

(2) to find how far the analogy mentioned in (1) persists under variation of the dot conditions; this is because the variation not only affects Λ_g but also dot-lead contact parameters t_1, t_2.

To proceed further, an exact knowledge of Λ_g is crucial. This in turn requires χ, which, however, is known only approximately for the localization → delocalization transition. As $Y - Y_0 \leqslant O(1/N)$ for AE cases (i) and (ii) as well as BE cases (iv) and (v) [see Eqs. (32) and (36)], Eq. (13) implies $\chi \sim \frac{1}{\xi^d(Y - Y_0)}$ in the large-N limit. Equation (19) along with Eqs. (32) and (36) then gives, for AE cases (i) and (ii) as well as for BE cases (iv) and (v), $\Lambda_g \propto \frac{\xi^d}{\Delta^2 N^2}$. To determine the size dependence of the proportionality factor, we numerically analyze the average peak height $\langle g\rangle$ (with $\langle . \rangle$ implying an ensemble average) for many system sizes for each transition in the AE and BE cases. [Following Eq. (27), the transition in $\langle g\rangle$ is governed by $N\Lambda_g$ only for a fixed set of the global constraints)]. As shown in Fig. 1, the above analysis for AE cases (i) and (ii) (corresponding to the Poisson-to-GOE and -GUE spectral transitions, respectively) for different sizes N

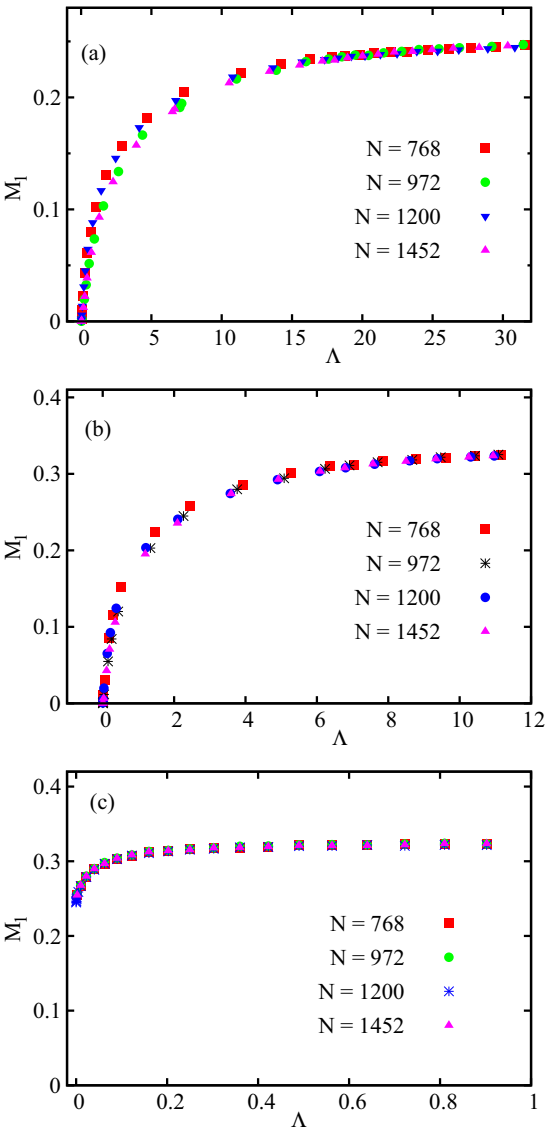

FIG. 1. (Color online) Size dependence of Λ_g for AE: Panels (a)–(c) depict the behavior of moment $M_1 \equiv \langle g \rangle$ with respect to Λ_g for AE dots connected to single-channel, symmetric leads for different matrix sizes N: (a) Poisson → GOE, (b) Poisson → GUE, and (c) GOE → GUE. The Λ_g used in the (a) and (b) is given by Eq. (38) with $\lambda_a = 1$ and by Eq. (41) in (c) with $\gamma = 1$. Note $\langle g(\infty) \rangle = 0.25$ in case (a) and 0.31 in cases (b) and (c) here, which is in agreement with Eq. (29).

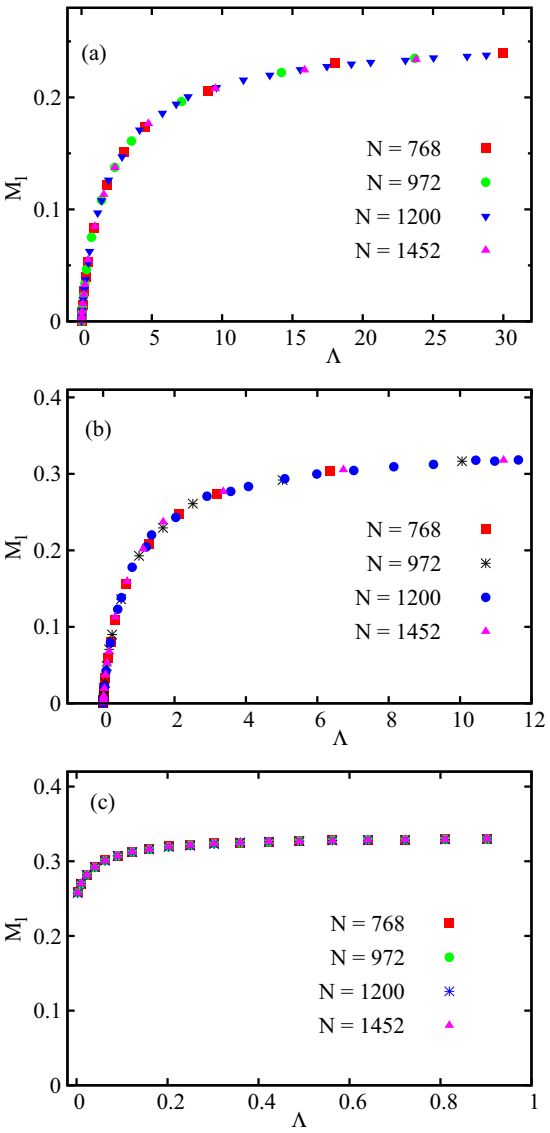

FIG. 2. (Color online) Size dependence of Λ_g for BE: Panels (a)–(c) depict the behavior of $M_1 \equiv \langle g \rangle$ with respect to Λ_g for the BE dots connected to single-channel, symmetric leads for different matrix sizes N: (a) Poisson → GOE, (b) Poisson → GOE, and (c) GOE → GOE. The Λ_g used in (a) and (b) is given by Eq. (39) with $\lambda_b \approx 15$ and by Eq. (42) in (c).

and disorder w indeed confirms that

$$\Lambda_{g,a}(E) \approx \frac{\lambda_a}{N} \frac{\xi^d}{\Delta^2 N^2} \tag{38}$$

with λ_a a constant. The $\langle g \rangle$ analysis for BE cases (iv) and (v) (corresponding to the Poisson-to-GOE and -GUE spectral transitions, respectively) for different N and c_1,c_2, however, suggests

$$\Lambda_{g,b}(E) \approx \frac{\lambda_b}{N} \frac{1}{4\pi c_1} e^{-E^2}, \tag{39}$$

with λ_b a constant and $\frac{\lambda_a}{\lambda_b} \approx 15$ (see Fig. 2). The theoretically predicted χ given by Eq. (13) therefore does not seem to work for BEs. But note that Eq. (19) remains valid for BE: Substitution of Eq. (36) along with the theoretically predicted

$$\Delta_{\text{local}}(E) = \frac{\sqrt{\pi}}{N} e^{E^2/2} \tag{40}$$

in Eq. (19) gives $\Lambda_{e,b}(E = 0) \approx \frac{1}{4\pi c_1}$ (see Eq. (12) of Ref. [9] for details about Eq. (40) with $\Delta_{\text{local}} = R^{-1}$, also see Ref. [12]). The validity of the later as the single parameter governing the eigenvalue fluctuations of BE has already been verified [9]; it was also successfully used to find the BE analog of the eigenvalue fluctuation measures of a given AE. Equation (19) along with Eq. (39) then suggests $\chi \approx \frac{\lambda_b}{N}$ for BE.

For the GOE → GUE transition, the eigenfunctions are extended with $\xi^d \approx \alpha/N$ (due to weak-localization effects,

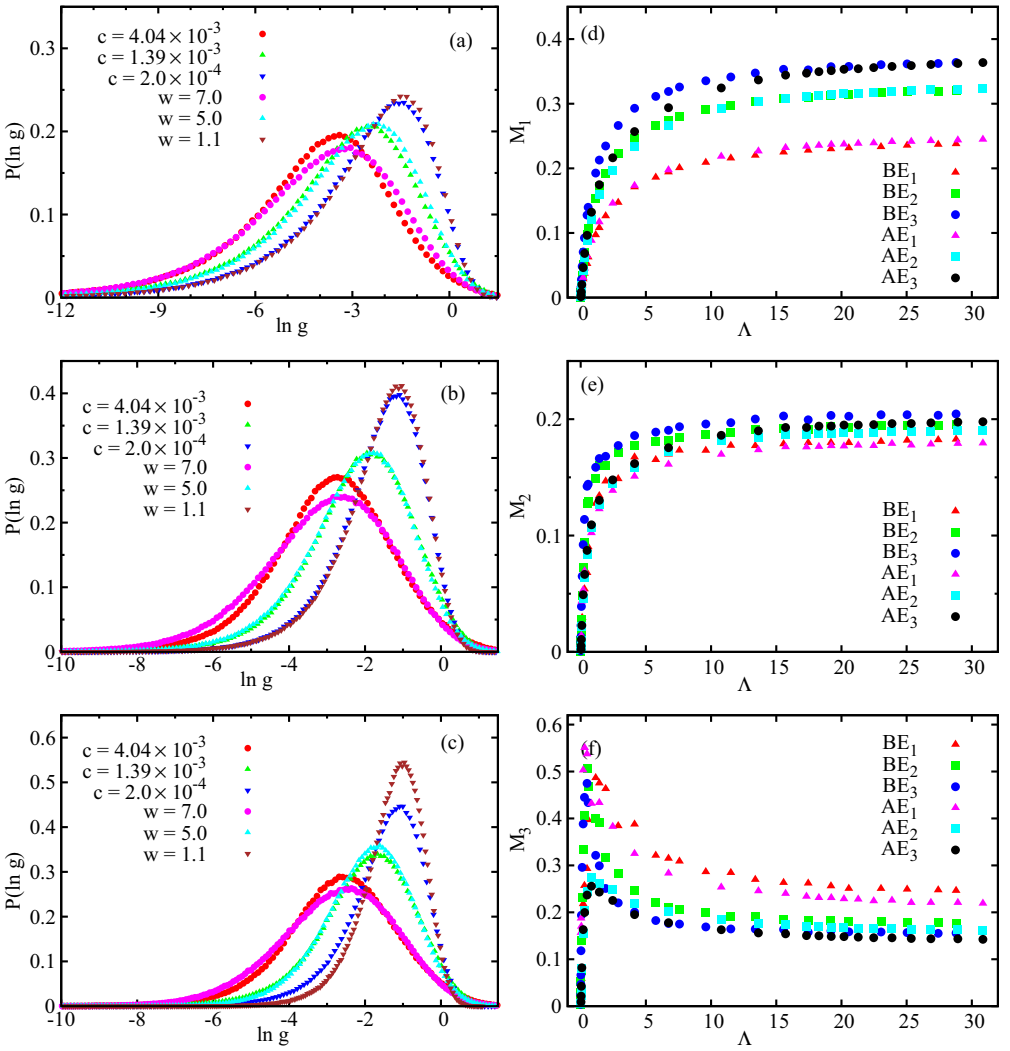

FIG. 3. (Color online) Dots with time-reversal symmetry: Poisson → GOE transition. Panels (a)–(c) show the $P(\ln g)$ behavior for the n-channels leads: (a) $n = 1$, (b) $n = 2$, and (c) $n = 3$. Each part depicts the behavior of three AEs [described by case (i) with ensemble complexity parameter Y given by Eq. (32)] and their BE analogs [case (iv) with Y given by Eq. (36) and $c_1 \equiv c$]. For different disorders of the AE case (i), the numerics gives following values: (1) $W = 7.0, F(0) \approx 0.128, I_2^{\rm typ} = 0.011, N\Lambda_g = 1.489$; (2) $W = 5.0, F(0) \approx 0.15, I_2^{\rm typ} = 0.0056, N\Lambda_g = 4.018$; (3) $W = 1.1, F(0) \approx 0.27, I_2^{\rm typ} = 0.0026, N\Lambda_g = 28.04$, where $F(E) = (N\Delta(E))^{-1}$ and Λ_g is obtained from Eq. (38) along with $\lambda_a = 1$, $F(E) = (N\Delta(E))^{-1}$, and $I_2^{\rm typ} = \xi^d$, which gives $\Lambda_{g,a} = F^2/(NI_2^{\rm typ})$. Using Eq. (39) with $\frac{\lambda_a}{\lambda_b} \approx 15$, it is easy to check that the BE analogs shown in the figure for each disorder satisfy the theoretical condition given by Eq. (43). Panels (d)–(f) depict the behavior of moments $M_k(\Lambda_g)$, $k = 1 - 3$; AE_n and BE_n refer to the AE and BE dots connected to the leads with n channels.

α varies from GOE to GUE). Equation (13) then gives $\chi = 1$, which in turn implies, from Eq. (19), $\Lambda_g = \Lambda_e$ for both AE case (iii) and BE case (vi). Equation (19) and (12) along with Eq. (33) then lead to Λ_g for AE case (iii),

$$\Lambda_{g,a}(E) \approx \frac{\xi^{2d}}{2\gamma\Delta^2 N^3} \ln|\cos(\phi) + \sin(\phi)|. \tag{41}$$

As shown in Fig. 1(c) for AE case (iii) with different N, the crossover in $\langle g \rangle$ is well described by Eq. (41). Similarly, Λ_g for BE case (vi) can be obtained from Eqs. (19) and (37),

$$\Lambda_{g,b}(E) \approx \frac{1}{8c_2 N^2 \Delta_{\rm local}^2}. \tag{42}$$

Numerical analysis of the spectrum in this case shows that $\Delta_{\rm local}(E)$ is almost constant during the crossover and can be well described by the GOE initial state $\Delta_{\rm local}(E) = \frac{1}{\pi\nu}\sqrt{2\nu N - E^2}$ with $\nu = 1/2$. This gives $\Lambda_{g,b} \approx \frac{1}{2c_2\pi^2 N}$; as shown in Fig. 2(c), the $\langle g \rangle$ analysis for different N of BE case (vi) confirms that this as a crossover parameter.

Note that a GOE → GUE crossover in a dot ensemble similar to BE dots was studied in Refs. [2,13], too, with their crossover parameter $\tau = \frac{\langle H_{\rm break}^2 \rangle}{\Delta^2}$ with $H_{\rm break}$ as the symmetry-breaking part of the dot Hamiltonian. Using τ as the crossover parameter, one finds $\tau_{\rm BE} = \frac{1}{\pi^2 Nc}$ for BE case (vi), thus differing from $\Lambda_{g,b}$ only by a constant $1/2$ [Eq. (42)]. For AE case (iii), however, $\tau_{\rm AE} = \frac{16N\phi^2}{\pi^2}$, which differs slightly from $\Lambda_{g,a}$ in the large-ϕ regime.

With Λ_g for AE and BE given by Eqs. (38), (39), (41), and (42), we can now proceed to verify the AE-BE analogy. To investigate objective (1), we numerically analyze and

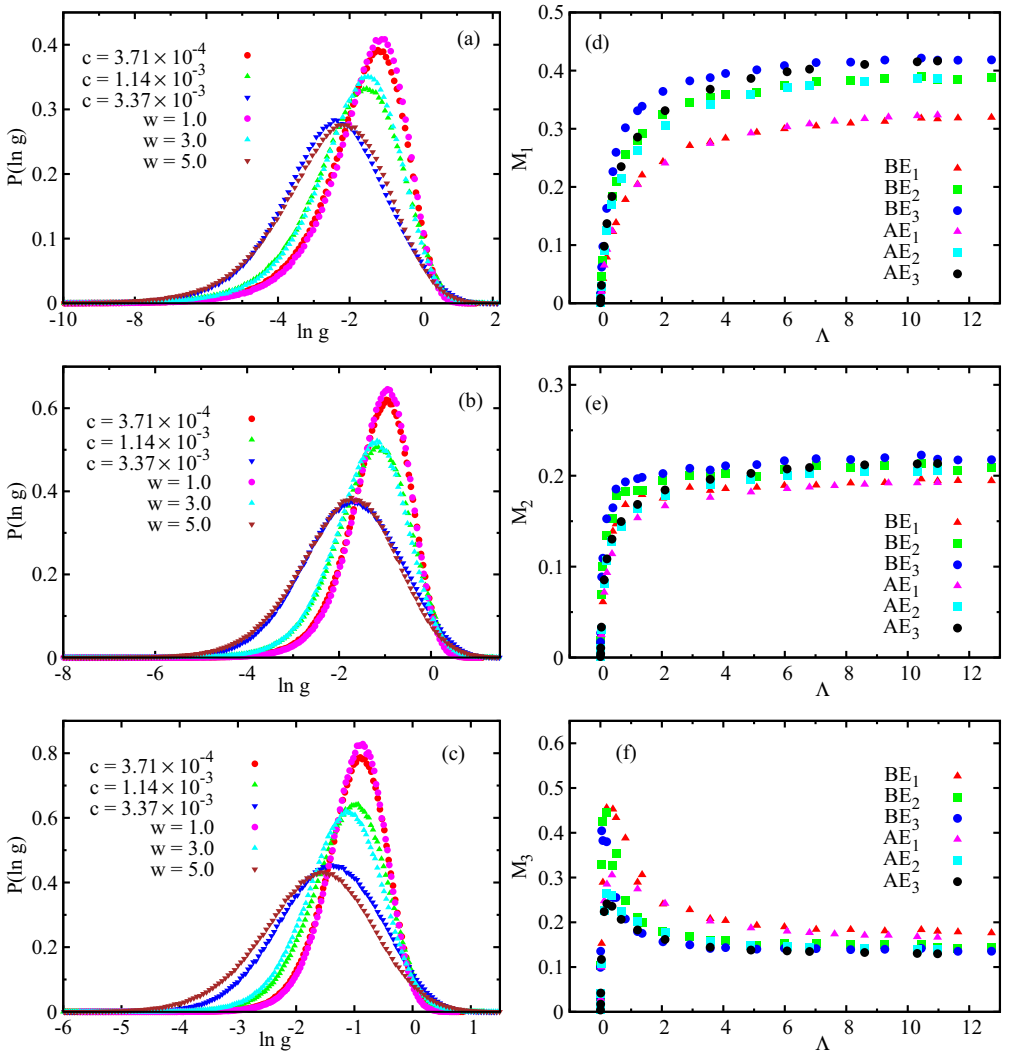

FIG. 4. (Color online) Dots without time-reversal symmetry: Poisson → GUE transition. Here again panels (a)–(c) show the $P(\ln g)$ behavior for the n channels leads: (a) $n = 1$, (b) $n = 2$, and (c) $n = 3$. Each part depicts AE case (ii) corresponding to three different values of the diagonal disorder w (with $\phi \neq 0$) and the BEs represented by the case (v) (for three different $c = c_1 = c_2$), respectively. The numerically obtained values for each AE case with $N = 1200$ are as follows: (1) $W = 1.0, F(0) \approx 0.28, I_2^{\rm typ} = 0.0018, N\Lambda_g = 43.56$; (2) $W = 3.0, F(0) \approx 0.19, I_2^{\rm typ} = 0.0026, N\Lambda_g = 13.89$; (3) $W = 5.0, F(0) \approx 0.15, I_2^{\rm typ} = 0.0048, N\Lambda_g = 4.69$, where $F(E) = (N\Delta(E))^{-1}$ and Λ_g is obtained from Eq. (38) along with $\lambda_a = 1$, $F(E) = (N\Delta(E))^{-1}$ and $I_2^{\rm typ} = \xi^d$, which gives $\Lambda_{g,a} = F^2/(NI_2^{\rm typ})$. Again, using Eq. (39) with $\frac{\lambda_a}{\lambda_b} = 5$, one can verify that the BE analogs for each disorder case satisfy the theoretical condition given by Eq. (43). Panels (d)–(f) depict the behavior of moments $M_k(\Lambda_g)$, $k = 1 - 3$; AE_n and BE_n refer to the AE and BE dots connected to the leads with n channels.

compare $P_g(g)$ for a fixed Λ_g as well as t_1,t_2 for AE with its theoretically predicted BE analog for each of the three types of transitions. As Λ_g for both ensembles is energy dependent, $P_g(g)$ should, in principle, be compared at a precise energy. For numerical analysis, however, one needs to consider averages over an optimized energy range δE (sufficiently large for good statistics while mixing of different statistics is kept at a minimum). We exactly diagonalize large ensembles of about 10^4 matrices of size $N = 1200$ with wave functions taken from a range δE, centered at $E = 0$ and of size 10% of the bandwidth, which gives approximately 121 levels for each case. The localization length $\xi(E)$ required to determine $\Lambda_{g,a}$ for AE is numerically obtained from the eigenfunctions in the neighborhood region of $E = 0$: $\xi^d(E) \propto (I_2^{\rm typ})^{-1}$ ([14]) with $I_2^{\rm typ}$ as the typical value of the inverse participation ratio I_2 of the eigenfunctions $I_2^{\rm typ} = \exp\langle \ln I_2 \rangle$ with $I_2 = \sum_n |\psi_n|^4$ for an eigenfunction ψ. The BE analog at $E = 0$ is then obtained by using Eqs. (36)–(39) along with the condition

$$\Lambda_{g,b}(E = 0) = \Lambda_{g,a}(E = 0). \tag{43}$$

Note that at $E = 0$ the BE analog given by the above condition is $c_1 = \frac{1}{60\pi} I_2^{\rm typ} \Delta_a^2 N^2$. Panels (a)–(c) of Figs. 3–5 show $P_g(\ln g)$ behavior for AE dots along with their BE analogs for each of the three types of crossover and the n-channel leads, $n = 1,2,3$; the close agreement in each case confirms our theoretical prediction.

Note that although the dot ensembles satisfying condition (43) may differ in their dot-lead contact characteristics t_1,t_2, the BE analogs of the AE dot in Figs. 3(a)–3(c) remain the same for each of the three lead types (see the caption of

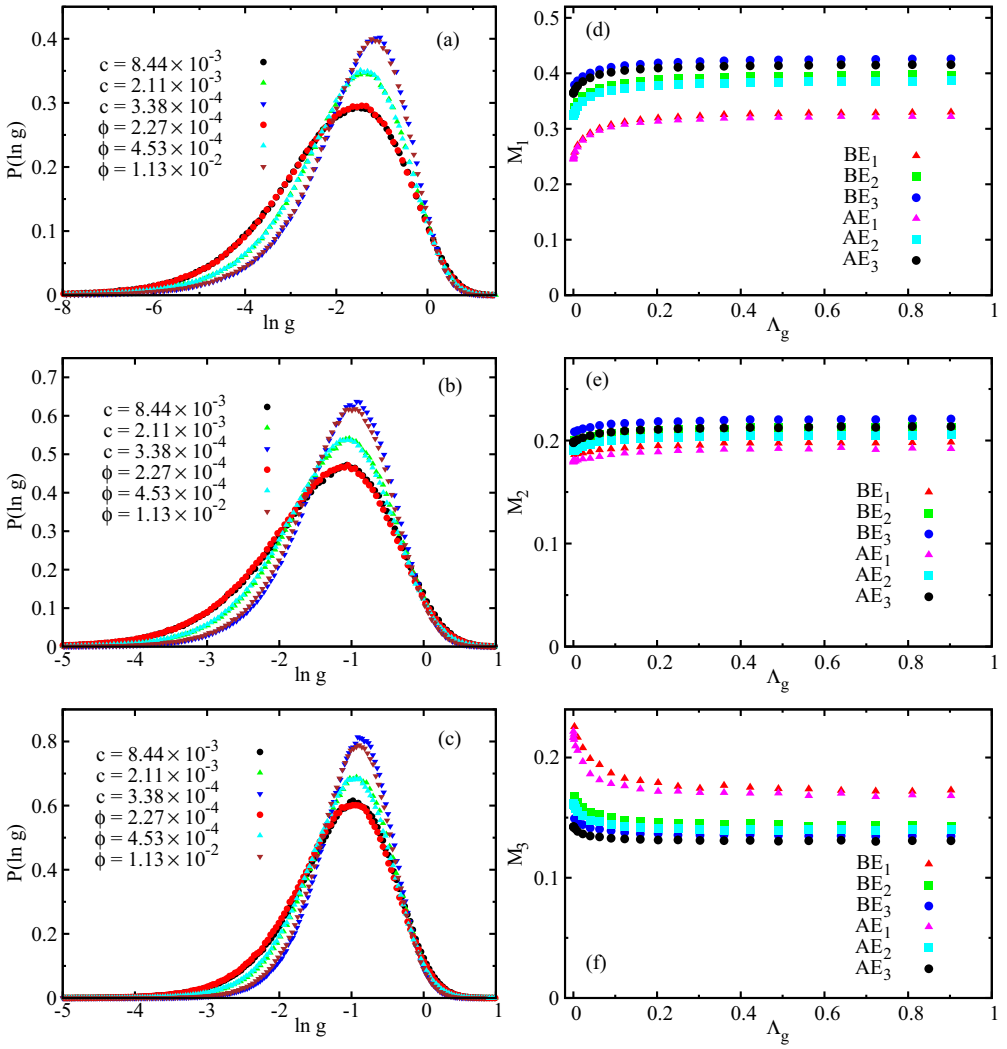

FIG. 5. (Color online) Dots without time-reversal symmetry: GOE → GUE transition. Here again the $P(\ln g)$ behavior is compared for the n-channels leads: (a) $n = 1$, (b) $n = 2$, and (c) $n = 3$ but the AEs now correspond to case (iii) with Y given by Eq. (33) (three different nonzero ϕ values) and BEs represented by the case (vi) with Y given by Eq. (37) (three different c_2 values), respectively. The numerics gives following values for each AE case (iii): (1) $\phi = 2.27 \times 10^{-3}, F(0) \approx 0.27, I_2^{\rm typ} = 2.4 \times 10^{-3}, \Lambda_g = 0.01$; (2) $\phi = 4.53 \times 10^{-3}, F(0) \approx 0.27, I_2^{\rm typ} = 2.1 \times 10^{-3}, \Lambda_g = 0.04$; (3) $\phi = 1.13 \times 10^{-2}, F(0) \approx 0.27, I_2^{\rm typ} = 1.9 \times 10^{-3}, \Lambda_g = 0.25$, where $F(E) = (N\Delta(E))^{-1}$ and Λ_g is obtained from Eq. (41). Again, using Eq. (42), one can verify that the BE analogs of AE case (iii) for each ϕ case, shown in (a), (b), and (c), satisfy the theoretical condition given by Eq. (43). Here again (d)–(f) depict the behavior of moments $M_k(\Lambda_g)$, $k = 1$–3 with respect to Λ_g; AE_n and BE_n refer to the AE and BE dots connected to the leads with n channels.

Fig. 3 for the AE and BE parameters). The same analogy also occurs in Figs. 4 and 5, too. This suggests a very weak sensitivity of $P_g(g)$ to dot-lead parameters t_1, t_2 [as the BE analog is obtained only by Eq. (43) and without matching t_1, t_2 for the two dots]. The apparent insensitivity may not seem surprising because the AE and BE ensembles used in Figs. 3–5 are in the weak-disorder regime in which their t_1, t_2 are expected to be of the same order due to similar localization tendencies [$t_1, t_2 \propto \Delta(E)$]. To gain an insight in t_1, t_2 influence on the AE-BE analogy, it is therefore imperative to analyze $P_g(g)$ behavior in the strong-disorder regime (note this also corresponds to small Λ_g) but very small g values along with numerical instability rules out the possibility of reaching a correct conclusion. Instead, alternative measures, e.g., the moments of $P_g(g)$, are more appropriate for the analysis in the weak-g regime.

To probe the parametric dependence for entire crossover, we compare the Λ_g variation of the moments M_n [defined in Eq. (25)] of AE with those of BE for each crossover type. As shown in panels (d)–(f) of Figs. 3, 4, and 5, the variation of M_n ($n = 1,2,3$) for AE is well in agreement with that of BE in the large-Λ_g range. As mentioned above, this analogy is not expected to survive in the small-Λ_g regime of Figs. 3 and 4 due to t_1, t_2 for the AE and BE dots differing for strong disorder. Contrary to expectations, however, almost no deviation is visible in case of the leads with single and two channels. This indicates the dominant influence of Λ_g, as compared to t_1, t_2, on $P_g(g)$ behavior. Alternatively, as compared to dot-lead characteristics, the dot characteristics influence the conductance fluctuations more significantly, even in generic dots. This behavior is expected in the Coulomb-blockade regime due to very small dot-lead contact regions.

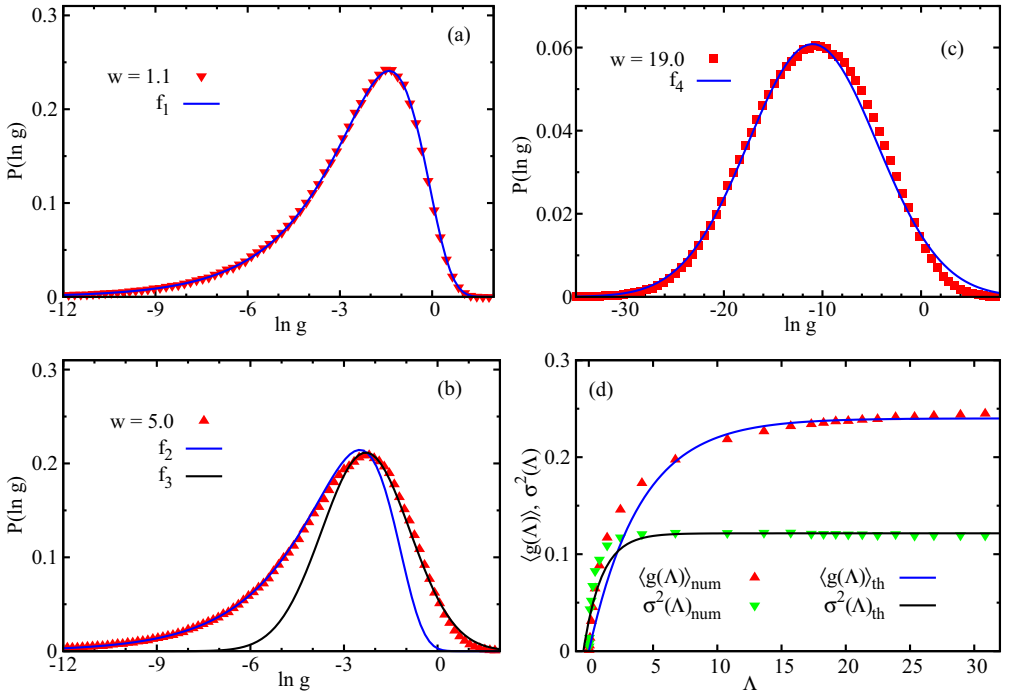

FIG. 6. (Color online) Comparison with theory: Dots with time-reversal symmetry. (a) Although the theoretical solution of Eq. (20) is obtained only as a series for the Poisson initial condition, Eq. (24) [obtained for $P(g,0) = \delta(g)$ initial condition] is well applicable for the case (i) in the weak-disorder limit [due to almost independence of the solution of Eq. (20) from the initial state in the large-Λ_g limit]. Here the function f_1 is given by Eq. (45) with $\tau_0 \approx 2$: $f_1(x) = 0.7977\exp(0.5x - 2e^x)$. (b) As disorder increases, Eq. (24) is applicable only in the lower part (below the peak) of the $P_g(g)$. The full distribution now seems to be a superposition of Eq. (45) with $\tau_0 \approx 2.33$ and a Gaussian; here f_2, f_3 are fitted functions with $f_2(x) = 1.33\exp(0.5x - 6.1e^x)$, $f_3(x) = \frac{0.75}{\sqrt{4\pi}}\exp[-(1/4)(x+2.3)^2]$. (c) For very strong disorder, i.e., $w = 19.0$, AE case (i) approaches a Gaussian distribution, referred to as f_4: $f_4(x) = \frac{1}{\sqrt{86\pi}}\exp[-(1/86)(x+11)^2]$. The approach to Gaussian behavior in the insulator regime is also suggested by previous studies [2]. (d) $\Lambda = 2N\Lambda_g$ governed evolution of average peak height $\langle g(\Lambda)\rangle$ and peak-height variance $\sigma^2(\Lambda)$ for AE case (i) for a single-channel lead with $N = 1200$ and their comparison with theory given by Eqs. (27) and (28): $\langle g(\Lambda)\rangle_{th} = 0.24(1.0 - \exp(-0.25\Lambda))$ and $\sigma_{th}(\Lambda) = 0.09(1.35 - \exp(-0.7\Lambda))$. Note that the large Λ_g results for both $\langle g(\Lambda)\rangle$ and $\sigma^2(\Lambda)$ agree with theoretical results (see Ref. [19]) for a GOE dot with single-channel symmetric leads: $\langle g(\infty)\rangle \approx 0.25$ and $\sigma^2(\infty) \approx 0.125$. As expected for symmetric leads, Eq. (29) then gives almost the same results for t_1 and t_2: $t_1 \approx t_2 = 0.25N$, which also agrees with Eq. (22).

The behavior of the moments in Figs. 1–5 also provides information about the equilibrium statistics, e.g., the GOE and GUE limits. The large-Λ_g limit (which corresponds to the end of the transition) of the figures suggests that

$$\langle g(\infty)\rangle = \left[\frac{N_c^2}{2(N_c+1)}\right], \quad \text{(GOE)}$$
$$= \left[\frac{N_c^2}{2N_c+1}\right], \quad \text{(GUE)}. \qquad (44)$$

These results are in agreement with previously known theoretical predictions for a dot [15] with symmetric leads with N_c channels. Using Eq. (29), the above GOE result can further be used to obtain the large-Λ_g limit of the dot-lead coupling characteristics: A comparison of Eq. (29) with the GOE result of Eq. (44) gives $t_1 = \frac{N_c^2 N}{4(N_c+1)}$. But Eq. (22) for symmetric leads with N_c channels gives $t_1 = N_c t_2 = \frac{\Delta}{\pi} N_c \kappa_l$. Combining these results together then gives $\kappa_l = \kappa_r = \frac{\pi N_c N}{4\Delta(N_c+1)}$.

An important point worth noting here is the independence of conductance statistics from the origin of complexity. For example, the GOE → GUE crossover for AE and BE has been brought about by different diffusion routes: For AE case (iii) it is the simultaneous variation of both the real and the imaginary parts of the nearest-neighbor off-diagonals of H; for BE case (vi) it is the variation of only the imaginary part of all off-diagonals. The AE-BE analogy for the entire crossover thus indicates an independence of the conductance statistics from the details of the diffusion route.

At this stage, it is very desirable to compare the $P_g(g;\Lambda)$ behavior for each crossover with the corresponding theoretical formulation. Unfortunately, due to technical complications, the explicit formulation for $P_g(g;\Lambda)$ is known only for one initial condition, namely $P(g,0) = \delta(g)$ [see Eq. (24)], and only when the crossover preserves the time-reversal symmetry. As both AE and BE considered here begin with Poisson or GOE initial conditions, their comparison with theory for an arbitrary Λ_g value is not feasible. But in the large-Λ_g limit, the crossover approaches the equilibrium and is expected to be free of the initial condition. The weak-disorder limit of the Poisson → GOE transition is therefore expected to agree with Eq. (24). Figure 6 compares our theoretical predictions with the numerics for the Poisson → GOE case for a single-channel AE dot with symmetric leads; from Eq. (44), $\langle g(\infty)\rangle = 0.25$ for this case which from Eqs. (27) and (22) gives $t_1 = t_2 = 0.25N$. Figures 6(a)–6(c) show the behavior of $P_g(\ln g)$ for

three cases $\Lambda_g = 28.04/N, 4.01/N, 0.02/N$ corresponding to disorders $w = 1.1, 5, 19$, respectively [Λ_g is given by Eq. (38) with $\Delta_{\rm local} = (NF(E))^{-1}, \xi^d = (I_2^{\rm typ})^{-1}$ with $(F(0), I_2^{\rm typ})$ as (0.27,0.0026), (0.15,0.0056), and (0.065,0.20) for $W = 1.1, 5.0, 19.0$, respectively]. The function f_1 in Fig. 6(a) is the theoretical predictions for $P(x)$ obtained from Eq. (24) with $x = \ln g$,

$$P_x(x) \approx \sqrt{\frac{\tau_0}{\pi}} \exp(0.5x - \tau_0 e^x). \tag{45}$$

Here $\tau_0 = \frac{N}{2t_2(1-e^{-0.5N\Lambda_g})}$, which gives $\tau_0 \approx 2$ for $w = 1.1$. As seen in Fig. 6(b), the lower arm of the distribution can be fitted by a function f_2, which is quite close to Eq. (45) with $\tau_0 \approx 2.33$ but the upper arm is well fitted by a Gaussian. For very strong disorder $w = 19.0$, the full distribution is fitted by a Gaussian. Thus, as expected, $P_g(g)$ for AE deviates from Eq. (45) with increasing disorder (i.e., decreasing Λ_g) and approaches a Gaussian distribution in the strong-disorder limit (i.e., $\Lambda_g \to 0$). As discussed in Sec. II C, the theoretical information about moments during crossovers preserving time-reversal symmetry is relatively easier to derive; Fig. 6(d) shows the numerical behavior of $\langle g(\Lambda)\rangle, \langle \sigma^2(\Lambda)$ along with functions $\langle g(\Lambda)\rangle_{th} = 0.24(1 - e^{-0.25\Lambda}), \sigma^2(\Lambda)_{th} = 0.09(1.35 - e^{-0.7\Lambda})$, where $\Lambda = 2N\Lambda_g$. With $\langle g(0)\rangle = 0$ and $t_1 = 0.25N$, the theoretical prediction given by Eq. (27) agrees almost exactly with $\langle g\rangle_{th}$. For variance, the function σ^2_{th} is very close to the self-consistent solution given by Eq. (28). Note that Eq. (25) is valid only for the time-reversal symmetry case [the numerical comparison is carried out only for case (i) of Sec. III)].

As discussed in Ref. [5], the inverse participation ratio $I_2^{\rm typ}$ is a function of Λ_g and therefore the condition (43) implies

$$I_{2,a}^{\rm typ} = I_{2,b}^{\rm typ} \tag{46}$$

[note, however, that Eq. (46) does not imply Eq. (43)]. Present numerics reconfirms the validity of Eq. (46) if Eq. (43) is satisfied and therefore provides new evidence in support of the complexity parameter-based formulation of the eigenfunction statistics of complex systems. The formulation in the case of both eigenvalues and eigenfunctions has been verified by previous numerical studies, too, e.g., a three-dimensional Anderson Hamiltonian (with and without spin-orbit coupling) [5,9,10], power-law random banded matrix ensembles, and kicked rotor [16].

V. SUGGESTED EXPERIMENT FOR COMPLEXITY PARAMETER ANALYSIS

The confirmation of our theoretical results of Ref. [4] by the numerical analysis presented above makes their experimental verification very desirable. In the past there have been many experiments to verify theoretical predictions of the peak-height distribution in chaotic dots [17]. The complexity parameter measurements, however, require the dots with variable system conditions, e.g., shape, size, disorder, magnetic field, and so on. Such measurements therefore can be carried out on disordered quantum dots with deformable shapes, coupled to bulk two-dimensional electron gas by individually adjustable point contact leads. As suggested in Ref. [18], such dot shapes can be formed by multiple teethlike gates. The shape can be changed by a small variation of the voltage on the inner gates without affecting the region near the quantum point contacts. This would allow one to follow a given peak as a function of shape and collect statistics without affecting the dot-lead contact characteristics. As shown by previous experiments [17], shape deformation techniques facilitate fabrication of ballistic dots with geometric and potential profiles which could generate classical dynamics ranging from integrable to chaotic. In these dots, their shape rather than disorder-induced scattering determines the properties of the phase coherence of the electrons. The complicated nature of multiple scattering from the boundaries also leads to randomization of the quantum operators and their statistical behavior can be modeled by generalized random matrix ensembles. (The success of standard random matrix ensembles in modeling the statistical behavior of chaotic and integrable systems has been well known for more than two decades. The appearance of generalized random matrix ensembles in the nonintegrable regime is also now known for many dynamical systems.)

The dots can again be formed by methods used in previous experiments, i.e., by gate depletion of a two-dimensional electron gas formed as the interface of a semiconductor heterostructure (e.g., GaAS/AlGaAs comprising a bulk GaAs substrate, a layer of AlGaAs, and a plain GaAs cap to prevent oxidation, with a ALGaAs layer grown on top of the GaAs layer by molecular-beam epitaxy) [17]. The lithographic dimensions of the dot are reduced by the gate voltages, which therefore control the effective area of the dot. The Fermi wavelength and the transport mean free path in the dot can be controlled by suitably choosing the mobility and particle density. By keeping the mean free path slightly larger or smaller than the dot size, the dynamics can be changed from ballistic to diffusive. Lithographic imperfections further ensure that each dot differs although all device parameters, e.g., area, Fermi wavelength, and electron density, are kept same. A similar difference can also be created by changing the impurity distribution within the dot while keeping the same doping strength.

Prior to measurements, it is necessary to ensure that the dot is in the Coulomb blockade regime which requires two conditions to be fulfilled: (i) the barriers must be large enough to keep the transmission small [this gives the condition $G \ll e^2/h$ (which corresponds to an isolated dot)] and (ii) the temperature T should be low enough so as not to wash out the charge quantization effects. As the charging energy, i.e., energy required to add a single electron in the dot, is $E_c = e^2/C$, this condition corresponds to $kT \ll E_c$. For a GaAs disk of radius $\sim$0.2 μm, typical $E_c \sim 10^3$ μeV and therefore the condition $kT \ll E_c$ can easily be satisfied at low temperatures.

For the observation of quantum coherence effects in closed dots, thermal fluctuations should usually be weaker than the single-particle mean level spacing $\Delta = \frac{\pi\hbar^2}{m^*A}$, where m^* is the effective mass of the electron and A is the quantum dot area. As $\Delta \sim 11$ μeV for a dot with an effective area $A \sim 0.3$ μm^2, it can usually be resolved at temperatures $T \sim 100$ mK (corresponding to $kT \sim 9$ μeV). The effective electronic temperature can be maintained by various techniques, e.g., dilution refrigeration; the minimum base temperature achieved through this method is $\sim$50 mK.

In GasAs dots, the electrons are typically confined ∼50–100 nm below the surface and their effective mass is $m^* = 0.067m_e$. The typical sheet density in these dots is $n_s \sim 4 \times 10^{11}$ cm^{-2}, which gives rise to a Fermi wavelength of $\lambda_F = \sqrt{2\pi/n_s} \sim 40$ nm and Fermi energy $E_f \sim 14$ meV. As the mobility μ_e in GaAs/AlGaAs heterostructures is in the range $\mu_e \sim 10^4$–10^6cm^2/V s, this results in a typical mean free path $l = (\mu_e/e)m^* v_F \sim 0.1$–$10$ μm (with v_F as the Fermi velocity). As in the previous experiments [17], Δ can be measured by applying a dc bias $V_{\rm dc}$ across the dot in the Coulomb blockade (CB) regime in addition to the ac bias. For $V_{\rm dc} \ll \Delta$, only the ground state is available for tunneling but, for $E_c > V_{\rm dc} > \Delta$, the excited states are also available and the spacings between the peaks at finite bias provide measurements of the level spacings between the discrete levels of the quantum dots. The differences in the gate voltage positions of the peaks therefore can be converted to level spacings of the dot Hamiltonian. The charging energy $E_c = \frac{e^2}{C_{\rm dot}}$, with $C_{\rm dot}$ as the dot capacitance, is obtained from the peak spacing ΔV_g^N between adjacent peaks (i.e., between the $N-1 \to N$ and $N \to N+1$ peaks) as the gate voltage V_g is swept: $E_c + s_N = e\eta\Delta V_g^N$ with s_N as the difference between the $N+1$ and N single-particle energies. Usually, $E_c \approx e\eta\Delta V_g$ (with the typical values of E_c being approximately 30–50 times the typical values of $\Delta = \langle S_N \rangle_N$). Here η, the gate-to-dot-capacitance ratio, is related to device temperature T, which can be measured from the width of the CB peak [the peakfull width at half maximum (FWHM) scales as akT with a a constant that differs for $kT > \Delta$ and $kT < \Delta$] $e\eta$FWHM $= 3.5kT$ at low temperature. The applied bias is kept less than the base temperature of the device, which ensures that the source and the drain are offset relative to each other by less than the thermal broadening of the Fermi surface. The lowest base temperature for the experiments on chaotic dots is ∼50 mK (i.e., 4.3 μeV), the ac bias voltage is varied in the range of 2–5 μeV, the level spacing Δ is typically of the order of 10–40 μeV, and the charging energy $E_c \sim 500$–1000 μeV. For generic dots, Δ is expected to be smaller due to weaker level repulsion.

Another important time scale for the conductance measurements is the time spent by the electron within the dot. In ballistic dots, the time of flight across the dot is roughly given by τ_c the ergodic time; the related energy scale $E_T = \hbar/\tau_c$ is termed the ballistic Thouless energy. The shape of the dot can be revealed in the conductance only if the electron undergoes multiple scatterings from the boundaries before its escape through the lead. This implies $\tau_{\rm escape} \gg \tau_c$, where $\tau_{\rm escape}$ is the mean escape time of the electron into the leads (equivalently, $\Gamma \ll E_T$). In case of a diffusive dot, the diffusive transport requires $l \ll L$ with L as linear size of the dot. This gives a time scale τ_D, the characteristic time scale for the electron to diffuse across the dot; the associated energy scale is known as the Thouless energy $E_c = \hbar/\tau_D$. For a diffusive dot, the impurity configuration can be revealed if $\tau_{\rm escape} \gg \tau_D$.

An ensemble of peaks can be collected by sweeping one of the gate voltages, say, V_{g1}, over several peaks (before conductance of point contacts changes) while keeping the others, say, V_{g2}, fixed. Incrementing V_{g2} at the end of each V_{g1} sweep changes the dot occupancy and/or dot geometry to yield a new set of statistically independent peaks on V_{g1} although the nature of wave-function dynamics may still remain unaffected (measured by average localization length). The latter can be ensured by verifying that a combination of such runs (over V_{g1}, V_{g2}) reproduce the peak height distribution $P_g(g)$ obtained by a single run for a fixed V_{g2}. The combination gives an ensemble of peak heights representing a dot characterized by $\langle V_{g2} \rangle$ [averaged over V_{g2} values used in the runs which leaves $P_g(g)$ behavior noticeably unaffected] besides other device parameters. (Note that this ensemble is equivalent to the one used in our numerics, obtained by taking the resonance peaks in an optimized energy range and over a number of matrices belonging to a specific ensemble density). An averaging over peak heights of the ensemble would give the average peak height $\langle g \rangle$ for the specific value of $\langle V_{g2} \rangle$. But the theoretical prediction in Eq. (27) gives

$$\Lambda_g = \frac{2}{N} \log\left[\frac{\langle g(\infty)\rangle - \langle g(0)\rangle}{\langle g(\infty)\rangle - \langle g\rangle}\right]. \tag{47}$$

Substitution of the experimentally obtained $\langle g \rangle$ in the above equation then can be used to extract Λ_g for the dot. Now, by further varying $\langle V_{g2} \rangle$, one can obtain a range of $\langle g \rangle$ values.

It has been observed in previous experiments that the peaks obtained by V_{g1} sweep are not all independent. But as Λ_g measurement requires a knowledge of $\langle g \rangle$ only, it can sufficiently reliably be measured from just a few peaks obtained by V_{g1} variation even for a fixed value of V_{g2}.

For experimental observation of the Poisson to GOE crossover, the initial dot shape can be chosen as a circular or rectangular billiard (which corresponds to integrable dynamics and Poisson spectral statistics). A slowly varying V_{g2} then can be used to approach a chaotic dot shape, e.g., stadium with GOE statistics. Similarly, Poisson-to-GUE crossover can be observed by imposing a magnetic field B on one of the inner gates and varying V_{g2} in a way to change dot shape again from an integrable to chaotic geometry. Similarly to V_{g1}, a nonzero B can be used to create a bigger ensemble of peaks for statistical analysis. But to observe GOE-GUE crossover, initial dot shape should also be chosen in the chaotic regime and B should be varied to reach the GUE regime. It is no longer necessary to change dot shape by changing V_{g2} although it can still be used to improve statistics.

Similar experiments can be performed on disordered dots where, instead of V_{g2}-induced shape deformation, the crossover can be brought about by increasing the doping of the semiconductor heterostructure. The ensemble of peaks in this case can be obtained by varying V_{g1} for a fixed doping strength and V_{g2}; the average over the peak values gives $\langle g \rangle$ for the specific value of doping and V_{g2}.

VI. CONCLUSION

To summarize, our numerical analysis, based on two prototype dots, confirms the analytical prediction of Ref. [4]: for a fixed set of global constraints on the system, the conductance peak-height distribution due to an isolated resonance is sensitive to the dot specifics only through the conductance complexity parameter Λ_g. The changing system conditions may lead to a variation of the conductance but the evolution route remains the same as long as global constraints are

the same irrespective of the specific details of the varying system conditions. This indicates a new type of universality of the conductance fluctuations: A large class of Coulomb blockade dots with different system conditions, e.g., shape, size, disorder, etc. (although same global constraints, e.g., symmetry, conservation laws, etc.), have the same distribution of the conductance peak heights if their Λ_g values are same. Each such class, characterized by Λ_g (besides global constraints) can appropriately be referred to as a nonequilibrium universality class of conductance fluctuations. The equilibrium class is approached as $\Lambda_g \to \infty$ and is characterized by the set of global constraints. As Λ_g varies continuously along the path from one equilibrium to another, with each point on this path corresponding to a universality class, this gives rise to a possibility of infinitely many such classes characterized by the complexity parameter besides a set of global constraints.

Note that the universality of conductance fluctuations in the context of chaotic or weakly disordered dots, i.e., those with ergodic or delocalized wave dynamics, has been well known for the past two decades and has been explained using parameter-free stationary random matrix ensembles (e.g., Wigner-Dyson ensembles) characterized by the underlying symmetry classes, i.e., a set of global constraints. These previously known classes are in fact the same as the equilibrium classes mentioned above. Our analytical work in Ref. [4] along with the present numerical work further extends the universality to dots with more generic system conditions, e.g., dots with nonintegrable or diffusive dynamics—those which can suitably be modeled by a system-dependent multiparametric Gaussian random matrix ensemble. Note that the universality of conductance fluctuations mentioned here is more generalized than the one reported earlier: Its characterization requires a knowledge of Λ_g, too, and not only the global constraints.

The implications of a possible Λ_g-based classification of generic Coulomb blockade dots is relevant not only for theoretical understanding but also for industrial purposes, e.g., self-assembled quantum dots [1]. It suggests Λ_g as the significant criteria to characterize the dot conductance and not the shape of the dot, disorder strength, and so on. But so far this suggestion is based only on the theoretical or numerical grounds and its experimental analysis or verification is very desirable. We believe that this should be feasible along the lines of the previous conductance experiments on chaotic or ballistic dots and have made suggestions in this regard in Sec. V. Although the present study is confined to the low-temperature Coulomb-blockade regime, we expect the existence of a complexity parameter formulation of $P_g(g)$ in other regimes, too.

Along with previous studies on the complexity-parameter-based formulations of the eigenvalues [9,10,16] and eigenfunctions [5,16], a similar formulation for a transport property, i.e., conductance, once again exposes the hidden web of rich, intricate connections among complex systems. Thus it seems that complexity wipes out most of the details, leaving the physical properties to be governed by the average behavior of only a few system parameters. In brief, complexity does seem to lead to universality.

APPENDIX A: APPROXIMATION USED IN EQ. (10)

The probability distribution of the components U_{nk}, $n = 1 \to N$, of an eigenstate, say, U_k, of an $N \times N$ Hamiltonian H, corresponding to an eigenvalue e_k and lying between ψ_n and $\psi_n + d\psi_n$, can be given as

$$P_\Psi(\psi_1,\ldots,\psi_N;Y) = \int f_k \rho(H,Y) dH, \tag{A1}$$

where $f_k = \delta(\Psi - U_k)\delta^{\beta-1}(\psi^* - U_k^*)$ and dH is the Haar measure in the Hermitian matrix space: $dH = \prod_j \prod_{m,n;m<n} |\lambda_m - \lambda_n|^\beta d\lambda_j dU_j$ with $\beta = 1,2$ for real-symmetric and complex Hermitian cases of H, respectively.

Partial differentiation of Eq. (A1) with respect to Y, subsequent substitution of Eq. (8), and partial integration leads to the diffusion equation for P_Ψ,

$$\frac{\partial P_\Psi}{\partial Y} = \frac{\beta^2}{4} \sum_{q=1}^{2} (L_q + L_q^*) \tag{A2}$$

with

$$L_1 = \sum_{n=1}^{N} \frac{\partial}{\partial \psi_n} [\psi_n T_{0nn}]$$

$$L_2 = \sum_{m,n=1}^{N} \frac{\partial^2}{\partial \psi_n \partial \psi_m^*} T_{1mn}, \tag{A3}$$

and

$$T_{rmn} = \sum_{j;j\neq k} \int \frac{(U_{nj} U_{mj}^*)^r}{(e_k - e_j)^2} f_k \, P_{N2}, de_j \, dU_j \, dU_j^* \tag{A4}$$

where $P_{N2} = P_{N2}(U_k, U_j, e_k, e_j)$ is the joint probability of all components of the two eigenvectors $U_j \equiv \{U_{nj}\}$ and $U_k \equiv \{U_{nk}\}$ $(n = 1 \to N)$ along with their eigenvalues e_j and e_k, respectively,

$$P_{N2} = \int \rho(H,Y) \prod_{m,n;m<n} |e_m - e_n|^\beta \prod_{l\neq j,k} de_l dU_l. \tag{A5}$$

Note that

$$P_\Psi = \int f_k P_{N2} \, de_j \, dU_j \, dU_j^*. \tag{A6}$$

Equation (A2) is derived exactly from Eq. (8). As the eigenvalues and eigenfunction are in general correlated, this along with the term $(e_j - e_k)^{-2}$ in the integral of Eq. (A4) makes it difficult to write L_k as a function of P_Ψ. But it can be simplified by noting that T_{rmn} is dominated by those terms in the $\sum_{j;\neq k}$ which correspond to the eigenvalues e_j close to e_k. Thus approximating $(e_k - e_j)^2 \approx \chi D_k^2$ with D_k as the local mean level spacing at energy e_k, one gets

$$T_{0mn} \approx \frac{\chi}{D_k^2} \sum_{j;j\neq k} \int f_k P_{N2} \, de_j \, dU_j \, dU_j^*, \tag{A7}$$

$$\approx \frac{(N-1)\chi}{D_k^2} P_\Psi, \tag{A8}$$

and

$$T_{1mn} \approx \frac{\chi}{D_k^2} \int \left(\sum_{j;j\neq k} U_{nj} U_{mj}^* \right) f_k \, P_{N2} \, de_j \, dU_j \, dU_j^*, \quad \text{(A9)}$$

$$\approx \frac{\chi}{D_k^2} (\delta_{mn} - U_{mk}^* U_{nk}) P_\Psi. \quad \text{(A10)}$$

Substitution of T_{0mn} and T_{1mn} in Eq. (A3) helps to reduce the evolution equation (A2) to Eq. (10). A more detailed analysis discussed in Ref. [5] suggests $\chi = 1$ for $\mu < \xi_k^d$, $\chi \sim (\mu/\xi_k^d)$ for $\mu > \xi_k^d$, with $\mu = (e^{2\eta(Y-Y_0)} - 1)^{-1}$, and ξ as the ensemble-averaged localization length of the eigenfunction U_k and d as the system dimension. The length ξ enters into the formulation due to its relation with typical intensity of a wave function: $|U_{nk}|^2 \sim \xi_k^{-d}$.

APPENDIX B: COMPLEXITY PARAMETER *Y*

Equation (7) appears to be complicated, with many parametric derivatives present on its right side. However, it is possible to map the multiparametric flow in the M-dimensional b space to a single parametric drift in another parametric space, say, y space, consisting of variables y_i, $i = 1 \to M$, where $M = [3 + \tilde{M}]\tilde{M}/2$. In other words, the generator T of the flow in the b space can be reduced to a partial derivative with respect to just one y-space variable, say, y_1,

$$T(y[b])\rho \equiv \left. \frac{\partial \rho}{\partial y_1} \right|_{y_2,\ldots,y_M}. \quad \text{(B1)}$$

The desired transformation $b \to y$ required to convert Eq. (7) into the form (8) can be obtained as follows. By using the definition $\frac{\partial}{\partial x} = \sum_{k=1}^{M} \frac{\partial y_k}{\partial x} \frac{\partial}{\partial y_k}$, with x as various b parameters, $T(b)$ can be transformed in terms of the derivatives with respect to y_1,

$$T\rho = \sum_k A_n \frac{\partial \rho}{\partial y_n}, \quad \text{(B2)}$$

where

$$A_n \equiv \sum_{k\leqslant l;s} \left[(g_{kl} - 2\gamma h_{kl;s}) \frac{\partial y_n}{\partial h_{kl;s}} - \gamma b_{kl;s} \frac{\partial y_n}{\partial b_{kl;s}} \right]. \quad \text{(B3)}$$

The Eq. (12) can be reduced in the desired form of Eq. (11) if the transformation $b \to y$ satisfies following condition:

$$A_n = \delta_{n1} \quad \text{for} \quad n = 1 \to M \quad \text{(B4)}$$

or, alternatively,

$$\frac{dh_{kl;1}}{2\gamma h_{kl;1} - g_{kl}} = \frac{dh_{kl;2}}{2\gamma h_{kl;2} - g_{kl}} = \cdots \frac{db_{ij;1}}{\gamma b_{ij;1}} = \frac{db_{ij;2}}{\gamma b_{ij;2}} \cdots \frac{dy_n}{-\delta_{n1}}, \quad \text{(B5)}$$

where the equality is implied for $k,l,i,j = 1,2,\ldots,N$.

The parameters y_n as a function of $h_{kl;s}$ and $b_{kl;s}$ can now be obtained by solving the set of conditions (B4) or, equivalently, Eq. (B5). For the case $(\gamma h_{kl;1} - g_{kl}) \neq 0, b_{kl;s} \neq 0$, Eq. (B5) gives (see Ref. [6] for the solution)

$$y_1 = -\frac{1}{4N^2\gamma} \ln \left[\prod_{k\leqslant l}{}' |1 - (2 - \delta_{kl}) h_{kl}/\gamma| \, |b_{kl}|^2 \right] + C_1, \quad \text{(B6)}$$

$$y_n = C_n \quad n > 1. \quad \text{(B7)}$$

Here $\prod'$ implies a product over nonzero b_{kl}, γ is an arbitrary parameter, giving the variance of the matrix elements at the end of the evolution (which can be scaled out without loss of generality), and C_n are constants of integration.

The solution given by Eq. (9) is not applicable in case one of the denominators becomes zeros during the evolution and it is necessary to consider alternative form of Eq. (B5). For example, if $b_{kl;s} = 0$ during the evolution, then Y can be obtained by rewriting Eq. (B5) in the following form:

$$\frac{dh_{kl;1}}{2\gamma h_{kl;1} - g_{kl}} = \frac{dh_{kl;2}}{2\gamma h_{kl;2} - g_{kl}} = \cdots \frac{d(b_{mn;1} + b_{mn;2})}{\gamma(b_{mn;1} + b_{mn;2})} = \cdots \frac{dy_1}{-\delta_{n1}}. \quad \text{(B8)}$$

A solution of the above equation gives

$$y_1 = \frac{-1}{\beta N^2 \gamma} \sum_{k\leqslant l} \left[\sum_{s=1}^{\beta} \ln|1 - \gamma(2 - \delta_{kl}) h_{kl;s}| + \ln \left| \sum_{s'=1}^{\beta} b_{kl;s'} + \delta_{b0} \right|^2 \right] + C_1, \quad \text{(B9)}$$

$$y_n = C_n \quad n > 1, \quad \text{(B10)}$$

with $\delta_{b0} = 1$ if both $b_{kl;1} = b_{kl;2} = 0$ or else $\delta_{b0} = 0$.

[1] R. J. Warburton, Nat. Mater. **12**, 483 (2013).
[2] Y. Alhassid, Rev. Mod. Phys. **72**, 895 (2000).
[3] C. W. J. Beeankker, Rev. Mod. Phys. **69**, 732 (1997).
[4] D. Dey and P. Shukla, Phys. Rev. B **84**, 195318 (2011).
[5] P. Shukla, Phys. Rev. E **75**, 051113 (2007).
[6] P. Shukla, J. Phys. A: Math. Theor. **41**, 304023 (2008).
[7] E. R. Mucciolo, V. N. Prigodin, and B. L. Altshuler, Phys. Rev. B **51**, 1714 (1995).
[8] P. Shukla, Phys. Rev. E **71**, 026226 (2005).
[9] P. Shukla, J. Phys: Condens. Matter **17**, 1653 (2005).
[10] R. Dutta and P. Shukla, Phys. Rev. E **76**, 051124 (2007).
[11] B. I. Shklovskii, B. Shapiro, B. R. Sears, P. Lambrianides, and H. B. Shore, Phys. Rev. B **47**, 11487 (1993).
[12] B. Shapiro, Int. J. Mod. Phys. B **10**, 3539 (1996).
[13] Y. Alhassid, J. N. Hormuzdiar, and N. D. Whelan, Phys. Rev. B **58**, 4866 (1998).
[14] R. N. Bhatt and S. Johri, Int. J. Mod. Phys.: Conf. Ser. **11**, 79 (2012).
[15] Y. Alhassid and C. H. Lewenkopf, Phys. Rev. Lett. **75**, 3922 (1995).

[16] R. Dutta and P. Shukla, Phys. Rev. E **78**, 031115 (2008).

[17] J. A. Folk, S. R. Patel, S. P. Godjin, A. G. Huibers, S. M. Cronenewett, C. M. Marcus, K. Campman, and A. C. Gossard, Phys. Rev. Lett. **76**, 1699 (1996); U. Sivan, R. Berkovits, Y. Aloni, O. Prus, A. Auerbach, and G. Ben-Yoseph, *ibid.* **77**, 1123 (1996); S. R. Patel, S. M. Cronenwett, D. R. Stewart, A. G. Huibers, C. M. Marcus, C. I. Duruoz, J. S. Harris, K. Campman, and A. C. Gossard, *ibid.* **80**, 4522 (1998); F. Simmel, T. Heinzel, and D. A. Wharam, Europhys. Lett. **38**, 123 (1997); R. O. Vallejos, C. H. Lewenkopf, and E. R. Mucciolo, Phys. Rev. Lett. **81**, 677 (1998).

[18] H. Bruus and A. D. Stone, Phys. Rev. B **50**, 18275 (1994).

[19] T. Rupp, Y. Alhassid, and S. Malhotra, Phys. Rev. B **65**, 193304 (2002).